ADVANCED MATERIALS
www.advmat.de

Bias-Free Solar Upcycling of Nitrate and Glycerol with Highly Efficient and Durable Organic Semiconductor-Based Photoelectrodes

*Yejoon Kim, Jee Hyeon Kim, Enok Lee, Sanseong Lee, Yoonsung Jung, Yunseo Jang, Inhyeok Oh, Jun Beom Hwang, Jungdae Lee, Kwanghee Lee, Hyunseob Lim, and Sanghan Lee**

The sustainable management of biodiesel byproducts, nitrate (NO_3^-) and glycerol, remains a critical environmental challenge, disrupting global nitrogen and carbon cycles. Addressing this issue from a materials science perspective, a bias-free photoelectrochemical (PEC) upcycling system based on the integration of functional energy materials is presented. A nickel-iron-phosphorus (Ni-Fe-P) electrocatalyst exhibits synergistic bi-functional activity for selective NO_3^- reduction and glycerol oxidation, driven by the redox dynamics of Ni and Fe and electronic modulation by phosphorus incorporation. Through a metal-foil encapsulation strategy, the catalyst is integrated with organic semiconductor (OS)-based photoanodes and photocathodes, forming a highly efficient OS-based PEC system capable of stable operation under continuous solar illumination. The individual photoelectrodes demonstrate photocurrent densities of +15.7 and−14.8 mA cm^{-2} under AM 1.5G conditions, while exhibiting remarkable stability with over 96% of initial performance retained after 60 h. To enable bias-free solar upcycling, a dual-photoelectrode PEC configuration is constructed, delivering a high reaction current of 11.04 mA cm^{-2} along with >95% Faradaic efficiencies and excellent selectivity for both ammonia (NH_3) and formic acid (FA) production. This work underscores the potential of materials-driven PEC platforms for selective solar chemical upcycling.

1. Introduction

In the Net Zero project envisioned by the International Energy Agency (IEA), biodiesel plays a critical role as among the diverse renewable energy sources intended to replace fossil fuels.[1] This significance arises from biodiesel's excellent compatibility with existing fossil fuel-based engine systems and its high energy density, rendering it a practical solution for long-distance transportation sectors, including aviation and shipping, where electric or hydrogen-based alternatives remain impractical.[2–4] However, large-scale biodiesel production inevitably increases nitrate (NO_3^-) emissions, driven by the use of chemical fertilizers during feedstock cultivation, as well as glycerol byproducts generated from the biodiesel synthesis process.[5,6] Both nitrate and glycerol function as environmental pollutants that disrupt the global nitrogen and carbon cycles and possess limited economic value as industrial waste.[7–9]

Y. Kim, E. Lee, S. Lee, Y. Jung, Y. Jang, I. Oh, J. B. Hwang, J. Lee, K. Lee, S. Lee
Department of Materials Science and Engineering
Gwangju Institute of Science and Technology (GIST)
123, Cheomdangwagi-ro, Buk-gu, Gwangju 61005, Republic of Korea
E-mail: sanghan@gist.ac.kr

S. Lee, K. Lee, S. Lee
Research Institute for Solar and Sustainable Energies (RISE)
Gwangju Institute of Science and Technology (GIST)
123, Cheomdangwagi-ro, Buk-gu, Gwangju 61005, Republic of Korea

The ORCID identification number(s) for the author(s) of this article can be found under https://doi.org/10.1002/adma.202507698

DOI: 10.1002/adma.202507698

S. Lee, K. Lee
Heeger Center for Advanced Materials (HCAM)
Gwangju Institute of Science and Technology
123, Cheomdangwagi-ro, Buk-gu, Gwangju 61005, Republic of Korea

J. H. Kim, H. Lim
Department of Chemistry
Gwangju Institute of Science and Technology (GIST)
123, Cheomdangwagi-ro, Buk-gu, Gwangju 61005, Republic of Korea

J. H. Kim, H. Lim
Center for Quantum Conversion Research (QCR)
Institute for Basic Science (IBS)
123, Cheomdangwagi-ro, Buk-gu, Gwangju 61005, Republic of Korea

H. Lim
Department of Semiconductor Engineering
Gwangju Institute of Science and Technology (GIST)
123, Cheomdangwagi-ro, Buk-gu, Gwangju 61005, Republic of Korea

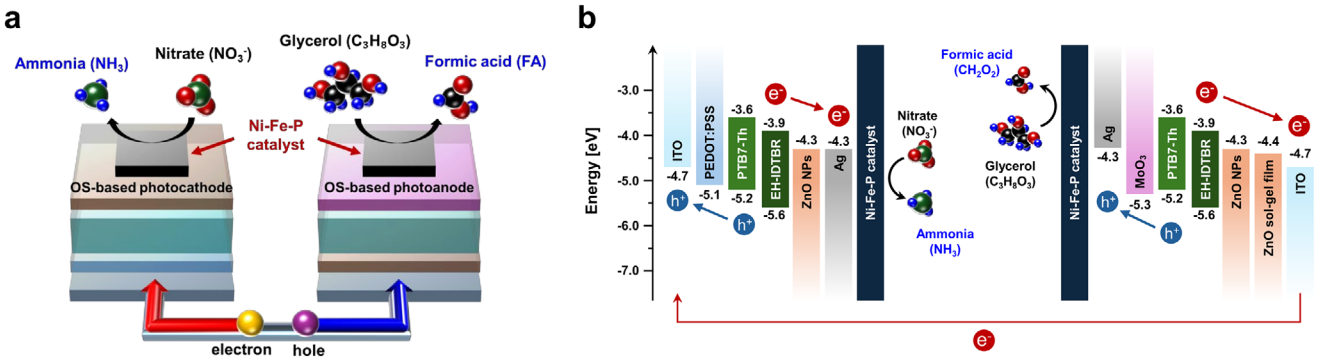

Figure 1. Design of OS-based bias-free solar upcycling system. a) Schematic illustration of a bias-free PEC upcycling system designed for the simultaneous conversion of nitrate to ammonia and glycerol to formic acid. b) Energy level diagram of the OS-based upcycling system. Vacuum energy levels and redox potentials were adapted from previously reported literature.[48–52]

To address this issue, electrochemical upcycling using renewable energy-based electrocatalysts has attracted significant attention.[10–16] It promotes the NO_3^- reduction reaction (NO_3RR) and glycerol oxidation reaction (GOR), converting environmental pollutants into high-value chemicals. Under relatively mild reaction conditions, NO_3^- can be upcycled into ammonia (NH_3), an essential substance in agriculture and chemical engineering, while glycerol can be transformed into high-value carbon compounds such as formic acid (FA), oxalic acid (OA), and 1,3-dihydroxyacetone (DHA), which are key chemicals in the pharmaceutical and cosmetics industries.[17–21] Electrochemical upcycling technology holds significant industrial value, but challenges remain in improving the reaction selectivity of NO_3RR and GOR and optimizing their suitability for renewable energy utilization.[22–25]

Nickel-iron (Ni-Fe) based catalysts have been reported to exhibit high selectivity for the conversion of NO_3^--to-NH_3 and glycerol-to-C1/C2 products, underscoring their strong potential for bi-functional activity in NO_3RR and GOR.[26–30] Chen et al. demonstrated that Ni-Fe alloy nanoparticles achieved 90.6% NH_3 selectivity and 74.8% Faradaic efficiency, attributable to the synergistic effects of strong NO_3^- adsorption and enhanced NH_3 formation.[31] Santana et al. further reported that Ni-Fe alloys in alkaline environments create an electronic structure conducive to C—C bond cleavage at the catalyst surface, resulting in high Faradaic efficiency for C2 and C1 products.[30] However, studies simultaneously employing Ni-Fe-based catalysts for both NO_3RR and GOR remain scarce, primarily due to the high corrosivity of Ni–Fe combinations, which hinders the long-term maintenance of reaction selectivity. In this context, Ni-Fe-P catalysts incorporating phosphorus have garnered attention due to their excellent corrosion resistance and higher conductivity compared to other transition metal compounds.[32,33] Specifically, the P-sites on the catalyst surface, which exhibit δ^- charges due to bonding with metals of different electronegativities, act as reversible adsorption sites of hydrogen ions, effectively facilitating the hydrogenation processes involved in NO_3^--to-NH_3 conversion and glycerol oxidation.[34–37]

In parallel, photoelectrochemical (PEC) systems represent a promising strategy for achieving renewable energy-based electrochemical upcycling. Photoelectrodes in usual PEC systems, which generate electron-hole pairs through light harvesting and participate in catalytic reactions, maximize the suitability of upcycling systems for renewable energy utilization.[38–43] Among these, organic semiconductor (OS)-based photoelectrodes are considered promising candidates for realizing bias-free solar upcycling systems due to their excellent light absorption properties and photoexcited charge carrier behaviors, which result in high photovoltage and photocurrent density.[44–46] Nonetheless, the chemical instability of OS materials in aqueous electrolytes has posed a significant barrier to their practical deployment in PEC applications. In our previous work, we demonstrated that metal foil encapsulation methods effectively blocks electrolyte penetration while enhancing electrochemical reaction kinetics, thereby ensuring the operational stability of OS-based photoelectrodes.[47]

In this study, we developed a PEC bias-free NO_3^- and glycerol upcycling system using Ni-Fe-P catalysts and OS-based photoelectrodes (**Figure 1**). The Ni-Fe-P catalyst exhibited bifunctionality, showing excellent activity for both NO_3RR and GOR. Compared to Ni-Fe catalysts, it demonstrated superior long-term operational stability and high reaction selectivity for NH_3 and FA production. The Ni-Fe-P bi-functional catalyst was integrated with OS-based photocathodes and photoanodes using a metal foil encapsulation method. Under AM 1.5G illumination, these electrodes achieved high photocurrent densities of −14.8 and 15.7 mA cm^{-2}, respectively, and maintained more than 96% of their initial current density after 60 hours of operation in alkaline electrolytes. Through the dual-photoelectrodes system, we successfully realized bias-free solar upcycling. It exhibited a high reaction photocurrent density of 11.04 mA cm^{-2} under AM 1.5G illumination without external voltage application and stably performed NO_3RR and GOR for over 20 h. The primary products of the OS-based bias-free solar system were NH_3 and FA, which demonstrated high Faradaic efficiencies over 92%, respectively, confirming the system's capability for selective upcycling. NH_3 and FA are valuable materials for agriculture, chemical engineering, renewable energy storage, and transportation. The upcycling system developed herein is anticipated to deliver substantial environmental benefits alongside considerable economic and industrial value. In particular, high selectivity of solar upcycling system toward both target products enhances its compatibility with industrial demands and scalable application, reinforcing its practical value in sustainable solar-driven chemical manufacturing.

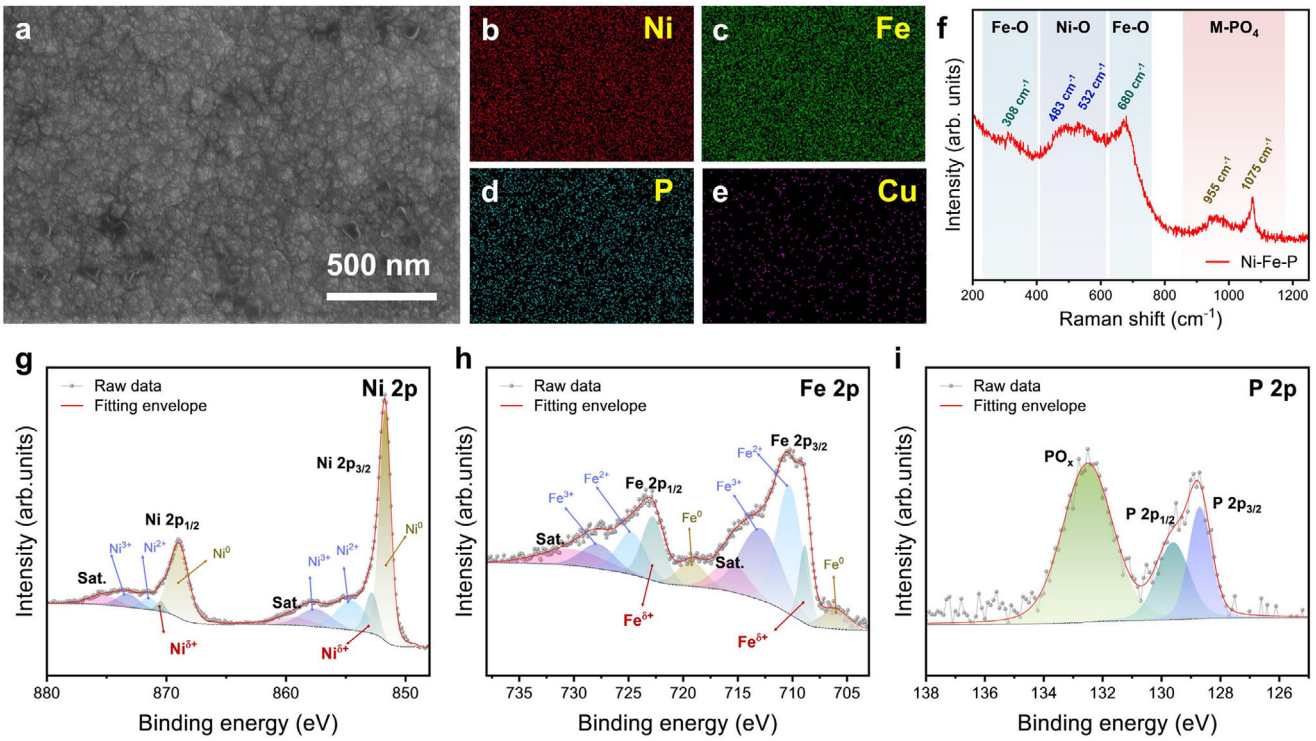

Figure 2. Material characteristics of the Ni-Fe-P catalyst deposited on the Cu foil. a) FE-SEM images and b–e) the corresponding EDS mapping images of the Ni-Fe-P catalysts. f) Raman spectrum of the Ni-Fe-P catalysts. g) Ni 2p, h) Fe 2p, and i) P 2p XPS spectra for the Ni-Fe-P catalysts.

2. Results and Discussion

2.1. Characterization of the Ni-Fe-P catalysts

The Ni-Fe-P catalyst was synthesized via electrodeposition using a three-electrode system on a Cu foil substrate. The Cu foil, Pt plate, and standard calomel electrode (SCE) were used as the working, counter, and reference electrodes, respectively. Electrodeposition was carried out at a constant current density of −10 mA cm^{-2} in an aqueous solution containing $NiSO_4$, $FeSO_4$, and $NaPO_2H_2$ as the Ni, Fe, and P precursors, respectively. After electrodeposition, the surface of the Cu foil visibly changed to a dark gray color (Figure S1, Supporting Information).

Field emission scanning electron microscopy (FE-SEM) was employed to examine the surface microstructure of the synthesized Ni-Fe-P catalyst. The results showed a smooth and uniform surface formed by the aggregation of multiple grains (**Figure 2a**). Notably, extending the deposition time did not significantly alter the surface morphology of the Ni–Fe–P catalyst (Figure S2, Supporting Information). Energy-dispersive X-ray spectroscopy (EDS) mapping of the sample deposited for 20 min revealed that Ni, Fe, P, and Cu were present on the catalyst surface at atomic proportions of 46.6%, 43.8%, 8.3%, and 1.3%, respectively (Figure 2b–e). The phosphorus content is consistent with values reported in previous studies on electrodeposited metal phosphides.[34,53] The phosphorus fraction on the catalyst surface remained nearly constant after 20 min of deposition (Figure S3, Supporting Information). Although the deposited Ni-Fe alloy contains a meaningful amount of phosphorus, its relatively low content allows the catalyst to retain the high electrical conductivity characteristic of metals, while also exhibiting features of metal phosphides, making it advantageous for electrocatalytic applications.[54,55]

To investigate the crystallographic structure of the Ni-Fe-P catalyst, X-ray diffraction (XRD) analysis was performed. No distinct diffraction peaks corresponding to the Ni-Fe-P alloy were observed, indicating that the alloy was deposited in an amorphous form without long-range atomic ordering on the Cu foil (Figure S4, Supporting Information). However, Raman spectroscopy revealed not only vibrational modes associated with metal oxides such as Ni—O and Fe—O, but also with phosphate species (PO_4^{3-}) including a broad band ≈ 955 cm^{-1} and a distinct peak at ≈1075 cm^{-1} (Figure 2f). To further clarify the origin of these features, we conducted comparative Raman measurements using Ni-P, Fe-P, and Ni-Fe control samples (Figure S5, Supporting Information). Control samples of Ni-P and Fe-P exhibited only broad Raman signals ≈950–1010 cm^{-1}, which can be attributed to the symmetric stretching mode (ν_1) of PO_4^{3-}, while no such signals were observed for Ni-Fe. In contrast, the Ni-Fe-P sample showed a distinct peak at 1075 cm^{-1} corresponding to the asymmetric stretching mode (ν_3), and this enhanced activation is likely induced by a change in the coordination environment around phosphorus, specifically through the coexistence of both Ni and Fe atoms that increase electrostatic asymmetry.[56,57] These results suggest the formation of phosphate-like species whose structure is modulated by surrounding metal atoms, supporting the existence of metal–P interactions even within the amorphous phase.

X-ray photoelectron spectroscopy (XPS) was conducted to analyze the surface chemical states of the Ni-Fe-P catalyst. The Ni 2p spectrum showed characteristic peaks of Ni^{3+} and Ni^{2+}

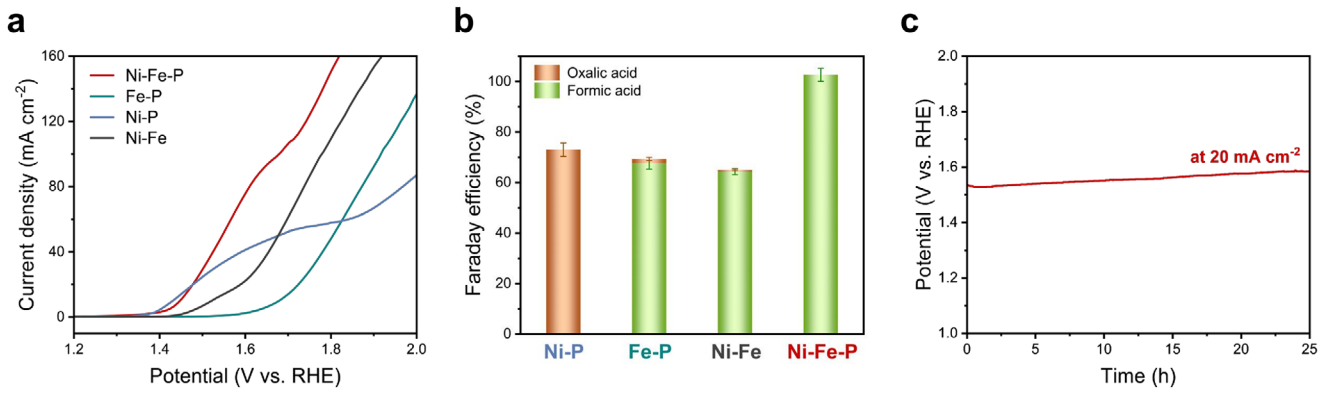

Figure 3. Electrochemical GOR performances of Ni-P, Fe-P, Ni-Fe, Ni-Fe-P catalysts. a) Polarization curves of catalysts in 1 M KOH + 0.1 M glycerol electrolyte at 50 mV s^{-1}. b) Faradaic efficiency for products by GOR at 10 mA cm^{-2}. Error bars denote standard deviation of the mean value (± SEM) of at least three ($n = 3$) separate measurements. c) CP curve of the Ni-Fe-P catalyst at 20 mA cm^{-2}.

accompanied by satellite peaks in both Ni $2p_{1/2}$ and Ni $2p_{3/2}$ regions, indicating partial surface oxidation and the formation of Ni—O bonds (Figure 2g). In addition, a strong metallic Ni^0 peak was observed, confirming the deposition of metallic Ni. Interestingly, peaks at 852.9 and 870.6 eV, which did not correspond to known oxidation states, were attributed to $Ni^{\delta+}$ ($0 < \delta < 2$), indicating the presence of Ni-P bonding.[58–60] The Fe 2p XPS spectrum displayed a similar trend, with peaks corresponding to Fe^{3+} and Fe^{2+} from partial oxidation, as well as a metallic Fe^0 peak (Figure 2h). Furthermore, a peak at 708.8 eV in the Fe $2p_{3/2}$ region was assigned to $Fe^{\delta+}$, providing evidence for Fe-P bonding.[61,62] These δ^+ peaks are attributed to electron transfer from the metal atoms to the more electronegative phosphorus atoms. In contrast, XPS analysis of a Ni-Fe alloy without phosphorus showed only peaks corresponding to oxidized and metallic species, with no δ^+ peaks associated with metal-phosphorus bonding (Figure S6, Supporting Information). The bonding between Ni/Fe and P was also confirmed in the XPS spectrum of the P 2p region, which exhibited two peaks at 129.7 eV (P $2p_{1/2}$) and 128.7 eV (P $2p_{3/2}$) corresponding to metal-P bonding, along with a peak at 132.4 eV attributed to P-O bonding due to surface oxidation (Figure 2i).[63,64] The clear splitting of the P 2p orbital strongly supports the existence of chemical bonding between phosphorus and the Ni/Fe species.

In conclusion, we successfully synthesized an amorphous Ni-Fe-P catalyst with partial phosphide characteristics via electrodeposition, by incorporating phosphorus into the Ni-Fe alloy. Raman and XPS analyses confirmed the formation of metal-phosphorus bonds and demonstrated that the addition of phosphorus led to electron redistribution at the catalyst surface, with partial positive charges on Ni and Fe and partial negative charge on P.

2.2. Electrochemical Performances of the Ni-Fe-P Catalysts

To investigate the influence of elemental combinations on the catalyst surface on GOR and NO_3RR, Fe-P, Ni-P, and Ni-Fe catalysts were also synthesized and tested (**Figure 3a**). For each sample, polarization curves were obtained in both 1 M KOH + 0.1 M glycerol electrolyte and 1 M KOH without glycerol (pH 13.8) (Figure S7a, Supporting Information). Additionally, chronopotentiometry (CP) measurements were conducted at a constant current density of 10 mA cm^{-2}, and the resulting electrolytes were analyzed via high-performance liquid chromatography (HPLC) to determine the products and reaction efficiencies (Figure 3b). All samples showed lower onset potentials in the presence of glycerol, indicating their activity toward GOR (Figure S7b, Supporting Information). Notably, for the three Ni-containing catalysts, a significant difference in onset potential between GOR and oxygen evolution reaction (OER) was observed. In these cases, the characteristic oxidation peak corresponding to the Ni^{2+} to Ni^{3+} transition disappeared, while a new peak appeared due to the potential-dependent (PD) oxidation mechanism of glycerol.[65,66] The PD mechanism, one of the principal pathways for glycerol oxidation on Ni-based catalysts, indicates that the Ni^{3+} species confirmed on the catalyst surface via XPS are actively involved in the electrocatalytic process. Moreover, the cleavage of C—C bonds in the glycerol molecule is promoted, facilitating its initial oxidation and enabling the effective production of oxalic acid (OA). Tafel slope analysis revealed that the Fe-P catalyst exhibited superior reaction kinetics for GOR, showing a smaller Tafel slope of 182 mV dec^{-1} compared to 285 mV dec^{-1} for Ni-P (Figure S7c, Supporting Information). The difference in reaction kinetics was reflected in the product distribution. Ni-P promoted the initial C—C bond cleavage via the PD mechanism and achieved a high OA production efficiency of 72%, but due to its slower kinetics, further oxidation to FA was limited. In contrast, Fe-P demonstrated fast reaction kinetics sufficient to oxidize glycerol to FA. However, due to its lower activity for the initial oxidation step and its high OER activity (Figure S7a, Supporting Information), the FA production efficiency was relatively low at 67%. These comparisons highlight the respective roles of Ni and Fe in the GOR process.

The effect of phosphorus on GOR activity was examined by comparing Ni-Fe and Ni-Fe-P catalysts. It is well known that the addition of Fe to Ni-based catalysts hinders the oxidation of Ni^{2+}, thereby promoting the oxidation of ions in the electrolyte.[67] Therefore, both Ni-Fe and Ni-Fe-P catalysts are expected to facilitate C—C bond cleavage through the PD mechanism driven by Ni, while benefiting from the fast reaction kinetics imparted by Fe. However, the two catalysts exhibited a

significant difference in onset potential (Figure 3a), and their Tafel slopes were 298 and 236 mV dec^{-1}, respectively, indicating that the presence of P significantly influences GOR activity (Figure S7c, Supporting Information). To further explore the role of phosphorus, cyclic voltammetry (CV) was performed at various scan rates (20, 50, 100, and 200 mV s^{-1}) in the non-faradaic region from −0.8 to −0.6 V versus SCE to determine the electrochemical active surface area (ECSA) (Figure S8, Supporting Information). Ni-Fe-P exhibited a much larger double-layer capacitance than Ni-Fe, indicating that the incorporation of P introduces additional electrochemical active sites on the bi-metallic Ni-Fe catalyst surface. The XPS results further supported this, revealing that the presence of phosphorus alters the valence states of the metal species, suggesting that these electronic changes contribute to the formation of GOR active sites.

In terms of product selectivity, Ni-Fe and Ni-Fe-P also showed clear differences. While Ni-Fe achieved FA production efficiency of 65%, Ni-Fe-P demonstrated a remarkable ≈100% FA production efficiency. These results suggest that Ni-Fe-P promotes GOR through a strong PD mechanism derived from Ni-P characteristics, and, with the aid of Fe, facilitates fast reaction kinetics for efficient glycerol-to-FA conversion.[68–70] Evidence supporting this mechanistic pathway was obtained from in situ Raman spectroscopy (Figure S9, Supporting Information), which provides direct insight into the surface redox processes of the Ni-Fe-P catalyst. Under OER conditions, a distinct NiOOH band at ≈470 cm^{-1} was observed, indicating Ni^{3+} formation. In contrast, under GOR conditions, the appearance of the NiOOH Raman band was notably suppressed even at higher potentials. Meanwhile, the glycerol-related peak at ∼1451 cm^{-1} gradually decreased, while the formate peak at ∼1335 cm^{-1} began to emerge and intensified with increasing potential. These results demonstrate that Ni serves as the primary active center for glycerol oxidation, undergoing rapid redox turnover, which prevents the accumulation of NiOOH species.

Moreover, the incorporation of phosphorus, which leads to the formation of a phosphide-like structure, provides enhanced long-term operational stability compared to conventional metal catalysts (Figure 3c; Figure S10, Supporting Information). In conclusion, Ni-Fe-P functions as a highly efficient and stable catalyst for the selective production of formic acid via glycerol oxidation. Post-GOR analysis (Figure S11, Supporting Information) revealed partial surface reconstruction with decreased P content, while residual metal–P bonds and stable Ni and Fe redox states were maintained, indicating preserved catalytic sites after prolonged operation.

The NO_3RR catalytic performance of Ni-P, Fe-P, Ni-Fe, and Ni-Fe-P was also evaluated. Polarization curves revealed that all samples exhibited higher current densities in the presence of NO_3^- in the electrolyte, indicating catalytic activity toward NO_3RR (**Figure** 4a; Figure S12a, Supporting Information). In particular, Ni-Fe-P achieved a current density of −20 mA cm^{-2} at potentials above 0 V versus reversible hydrogen electrode (V_{RHE}), exceeding typical values observed under hydrogen evolution reaction (HER)-dominant conditions (1 M KOH), thereby clearly demonstrating its excellent activity toward NO_3RR (Figure S12b, Supporting Information). Tafel slope analysis further revealed that all Fe-containing catalysts (Fe-P and Ni-Fe) showed lower Tafel slopes compared to Ni-P, suggesting that Fe enhances the NO_3RR kinetics (Figure S12c, Supporting Information). Indeed, prior studies have reported that abundant Fe^{2+} active sites effectively facilitate NO_3^- adsorption and reduction, and when coupled with elements such as Ni or Cu, which are efficient proton donors, the overall NO_3RR kinetics can be significantly enhanced.[71,72] Within this framework, the outstanding NO_3RR performance of Ni-Fe can be rationalized. Additionally, $Fe^{\delta+}$ active sites, formed in Fe-P bonding environments, are believed to promote spontaneous redox interactions that reduce NO_3^- near the catalyst surface. It may help overcome the high energy barrier associated with the rate-determining step of NO_3RR, the transition from adsorbed $^*NO_3$ to $^*NO_2$.[73] Therefore, Fe-P also functions as an effective NO_3RR catalyst. In contrast, while Ni-P exhibits a reduction peak in the presence of NO_3^- corresponding to the $^*NO_3$ to $^*NO_2$ transition, the reaction kinetics in that region appear to be sluggish.

CP measurements were conducted at −10 mA cm^{-2}, and the amount of generated NH_3 was analyzed. Ni-P demonstrated a higher NH_3 production efficiency (90.1%) compared to Fe-P (82.1%) and Ni-Fe (88.5%) (Figure 4b). Furthermore, the production efficiency of nitrite (NO_2^-), a major intermediate in nitrate reduction, was 10.7% for Ni-P, which is lower than that for Fe-P (19.1%) and Ni-Fe (14.6%). These findings indicate that Fe contributes to the efficient $^*NO_3$ to $^*NO_2$ conversion, while Ni plays a crucial role in the subsequent reduction of $^*NO_2$ to NH_3.[74,75] Moreover, Ni-Fe-P exhibited the highest NH_3 production efficiency of 99.6% and the lowest NO_2^- production efficiency of only 0.3%. The surface electronic structure modulation induced by metal-P bonding and the reversible protonation of P atoms characterized by the δ^- state appear to promote NO_3RR and NH_3 production.[76] Furthermore, the catalyst was stable for long periods of operation at −20 mA cm^{-2} (Figure 4c).

To investigate the structural evolution of the Ni–Fe–P catalyst during NO_3RR, in situ Raman spectroscopy was conducted under electrochemical operating conditions. Under open-circuit potential (OCP), a broad vibrational band corresponding to Ni—O bonds (≈570 cm^{-1}) was observed, suggesting the presence of partially oxidized Ni species (Figure 4d). Upon applying increasingly negative potentials (+0.2 to −0.4 V_{RHE}), the Ni—O signal gradually decreased in intensity, while new features assigned to Fe—O bonds (≈670 cm^{-1}) became increasingly pronounced. Importantly, the emergence of Fe—O vibrational features coincided with the progressive decrease of the symmetric stretching band of NO_3^- (≈1045 cm^{-1}) from −0.2 V_{RHE} (Figure 4f). Considering that no peaks were detected in this region under NO_3^--free conditions, and that the corresponding vibrational band gradually decreased over time at a constant potential of −0.2 V_{RHE}, but reappeared upon the reintroduction of nitrate, this signal can be unequivocally attributed to NO_3^- species (Figure 4e; Figure S13, Supporting Information). These observations strongly suggest that the oxidation of Fe is directly coupled to the electrochemical reduction of NO_3^-. Specifically, Fe^{2+} species appear to donate electrons to NO_3^-, promoting its conversion to NO_2^- through oxygen abstraction and leading to the formation of Fe^{3+}-O species as a reactive intermediate. Meanwhile, the gradual disappearance of the Ni—O peak with decreasing potential suggests that nickel undergoes a reversible electrochemical transition, possibly from

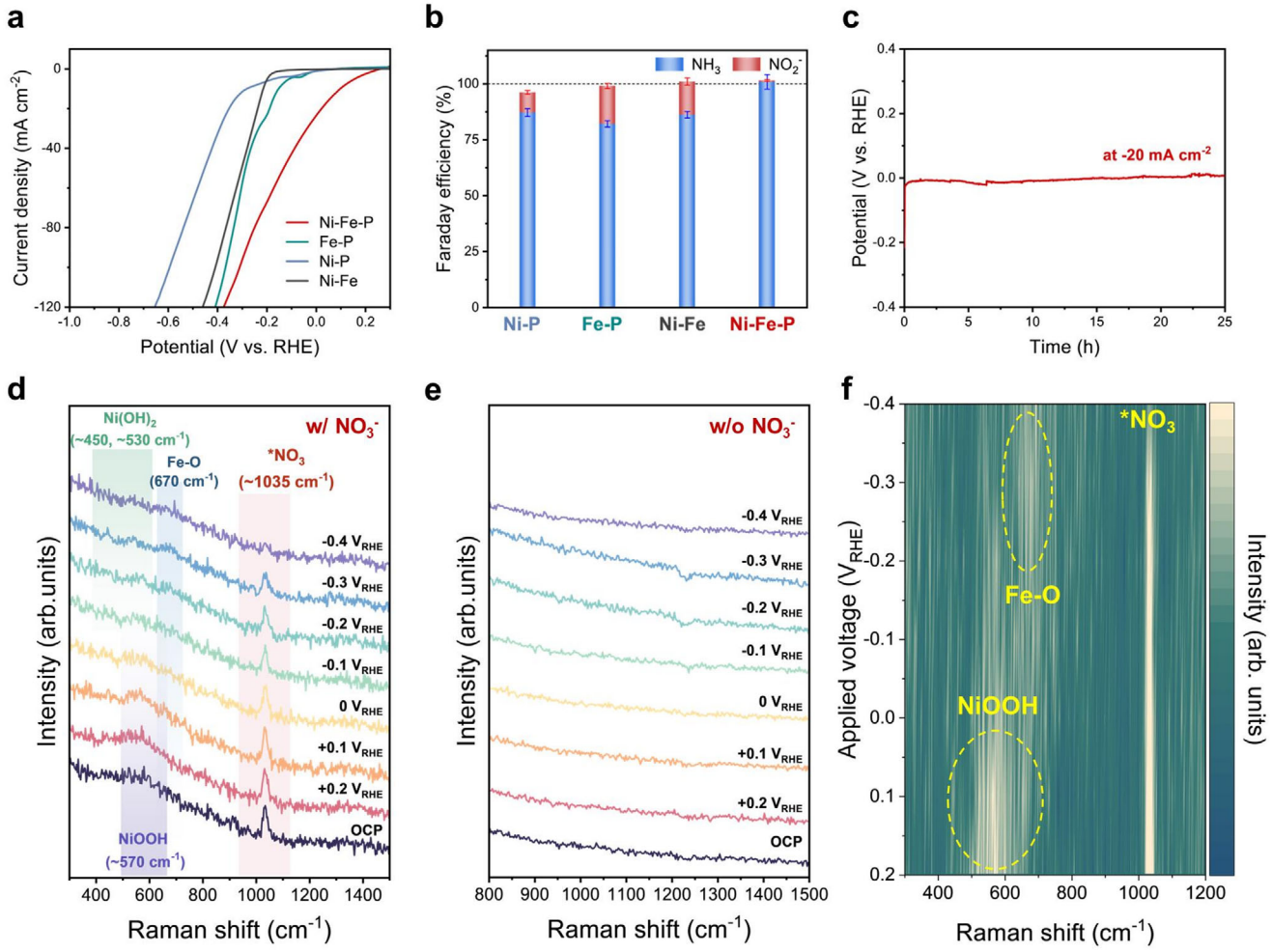

Figure 4. Electrochemical NO_3RR performances of Ni-P, Fe-P, Ni-Fe, Ni-Fe-P catalysts. a) Polarization curves of catalysts in 1 M KOH + 0.1 M KNO_3 electrolyte at 50 mV s^{-1}. b) Faradaic efficiency for products by NO_3RR at −10 mA cm^{-2}. Error bars denote standard deviation of the mean value (± SEM) of at least three ($n = 3$) separate measurements. c) CP curve of the Ni-Fe-P catalyst at −20 mA cm^{-2}. In situ Raman spectra of Ni-Fe-P at different applied potentials (d) with NO_3^- and (e) without NO_3^-. f) Contour mapping of in situ Raman spectra of Ni-Fe-P at different apploed potentials.

a more oxidized form such as NiOOH to a reduced hydroxide state like $Ni(OH)_2$ (≈450, ≈530 cm^{-1}).[77] Recent studies have reported that $Ni(OH)_2$ can serve as an effective hydrogenation site for the electrochemical reduction of NO_2^- to NH_3, facilitating multi-electron transfer steps involved in NO_3RR.[78,79] Indeed, NO_2^- reduction reaction (NO_2RR) experiments confirmed that catalysts containing Ni exhibited higher Faradaic efficiencies for NH_3 production, indicating their strong capability for converting NO_2^- to NH_3 (Figure S14, Supporting Information). Post-NO_3RR characterization further revealed nanoscale restructuring of the Ni-Fe-P catalyst surface and retention of metal–P bonding, demonstrating that the structural integrity and electronic environment of the active sites remain preserved after prolonged operation (Figure S15, Supporting Information). These findings indicate that the NO_3RR mechanism of Ni-Fe-P proceeds while maintaining metal–P bonding within the catalyst structure, suggesting that phosphorus remains integrated and continues to influence the electronic and catalytic properties during the reaction.

2.3. Photoelectrochemical Performances of the Ni-Fe-P Catalysts

For an efficient PEC upcycling system, both photoanode and photocathode were fabricated using OS bulk-heterojunction (PTB7-Th:EH-IDTBR) as photoabsorber layers. The photoelectrode fabrication process employed a metal foil encapsulation method, in which a homemade carbon paste was used as a conductive adhesive to electrically connect the Ni-Fe-P catalyst deposited on a copper foil (Ni-Fe-P/Cu foil) to the top electrode of the organic photovoltaic (OPV) device. This method effectively prevents electrolyte infiltration into the OS layer, thereby maximizing photoelectrode stability. Conventional and inverted OPVs were configured as the photocathode and photoanode, respectively (Figure S16, Supporting Information). Prior to photoelectrode assembly, the photovoltaic performance of each OPV devices was evaluated via *J–V* characterization (Figure S17, Supporting Information).

The Ni-Fe-P/Cu foil/OS-based photoanode was tested in 1 M KOH electrolyte with and without 0.1 M glycerol by recording polarization curves (**Figure 5a**). The PEC performance in

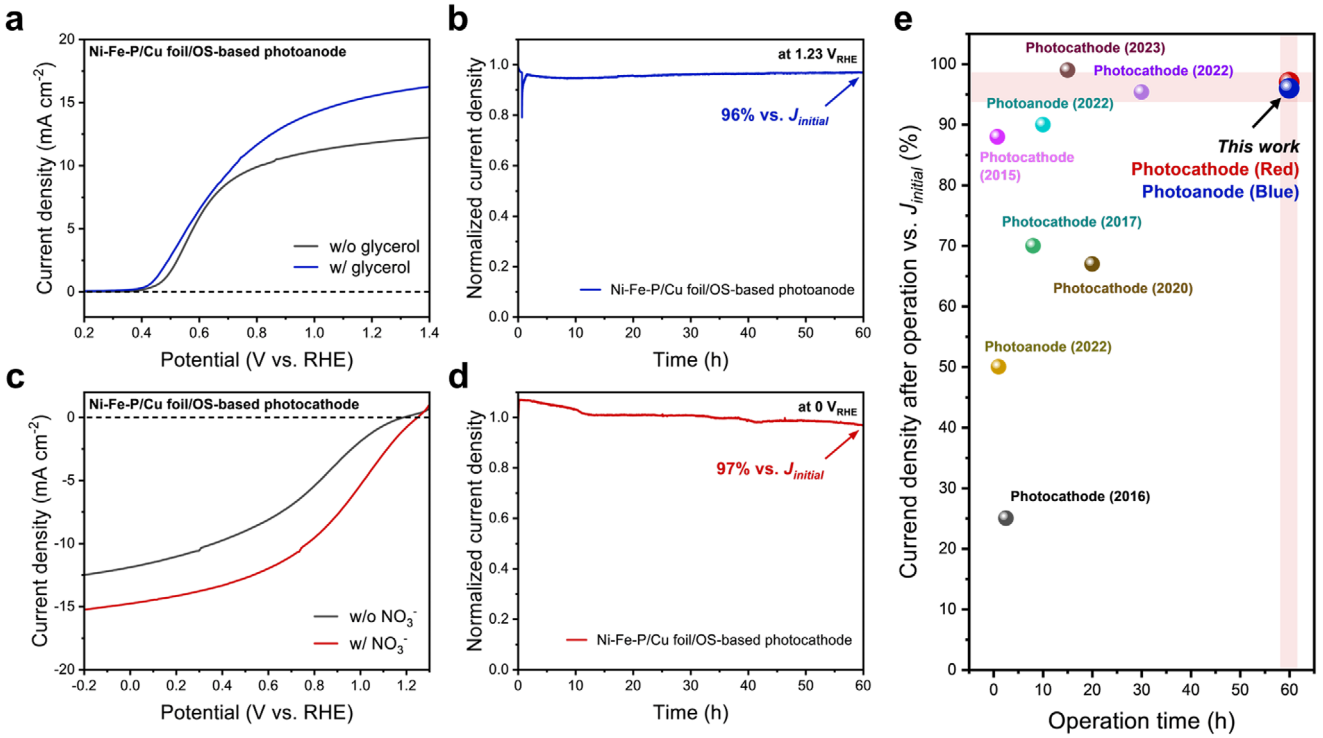

Figure 5. Photoelectrochemical GOR and NO_3RR performances of OS-based photoelectrodes. a) Polarization curves (scan rate: 50 mV s^{-1}) and b) CA curve at 1.23 V_{RHE} of the Ni-Fe-P/Cu foil/OS-based photoanode in 1 M KOH + 0.1 M glycerol electrolyte. c) Polarization curves (scan rate: 50 mV s^{-1}) and d) CA curve at 0 V_{RHE} of the Ni-Fe-P/Cu foil/OS-based photocathode in 1 M KOH + 0.1 M KNO_3 electrolyte. e) Operational stability comparison of current research and previously reported works.

glycerol-free electrolyte corresponds to OER activity, whereas in the presence of glycerol, it reflects GOR activity. The Ni-Fe-P/Cu foil/OS-based photoanode exhibited a low onset potential of ≈0.5 V_{RHE} for OER and 0.4 V_{RHE} for GOR. These values closely match the corrected potentials of the Ni-Fe-P catalyst's electrochemical activity (1.5 V_{RHE} for OER and 1.4 V_{RHE} for GOR), adjusted by the 1.02 V open-circuit voltage (V_{oc}) of the inverted OPV (Figures S7a and S17a, Supporting Information). It indicates that the homemade carbon paste successfully established an efficient electrical connection between the Ni-Fe-P/Cu foil and the inverted OPV without significant internal resistance or performance degradation. As expected from the electrochemical activity of the Ni-Fe-P catalyst, the Ni-Fe-P/Cu foil/OS-based photoanode exhibited enhanced photoelectrochemical performance in the glycerol-containing electrolyte. At 1.23 V_{RHE}, the photocurrent density reached 15.7 mA cm^{-2} in the presence of glycerol, compared to 11.9 mA cm^{-2} without glycerol, ndicating a preference for the GOR pathway over the OER. Furthermore, the photoanode showed remarkable stability, maintaining 96% of its initial photocurrent density after 60 h of continuous operation under chronoamperometric (CA) conditions at 1.23 V_{RHE} (Figure 5b).

For the Ni-Fe-P/Cu foil/OS photocathode, polarization curves were obtained in 1 M KOH electrolyte with and without 0.1 M KNO_3 (Figure 5c). Considering the NO_3RR and HER activity of the Ni-Fe-P catalyst and the V_{oc} of the conventional OPV (1.04 V), the photocathode was also confirmed to operate without internal charge loss (Figures S12a and S17b, Supporting Information). In the absence of KNO_3, the photocathode exhibited a current density of −11.9 mA cm^{-2} at 0 V_{RHE}, which increased to −14.8 mA cm^{-2} in the presence of KNO_3, reflecting the superior NO_3RR activity of the Ni-Fe-P catalyst. The CA curve showed that the photocathode retained 97% of its initial current density after 60 h of continuous operation at 0 V_{RHE}, demonstrating excellent long-term stability comparable to that of the photoanode (Figure 5d).

The high efficiency and durability of the OS-based photoelectrodes can be attributed to the combined effects of the excellent catalytic activity and durability of the Ni-Fe-P catalyst for both GOR and NO_3RR, the robustness of the metal foil encapsulation technique using homemade carbon paste, and the outstanding photovoltaic properties of the OS-based devices. The OS-based photoanodes and photocathodes developed in this study exhibit significantly improved operational time and stability compared to previously reported OS-based photoelectrodes (Figure 5e; Table S1, Supporting Information).[47,80–86]

2.4. Bias-Free PEC Solar Upcycling System

The highly efficient and durable OS-based photocathode and photoanode were integrated into a dual-photoelectrodes system to enable bias-free PEC upcycling, converting NO_3^- to NH_3 and glycerol to FA. The PEC and upcycling performance of this system was evaluated under illumination from a single LED light source with a large active area (AM 1.5G, 100 mW cm^{-2}, 15 × 15 cm^2). A two-electrode configuration was employed, with the

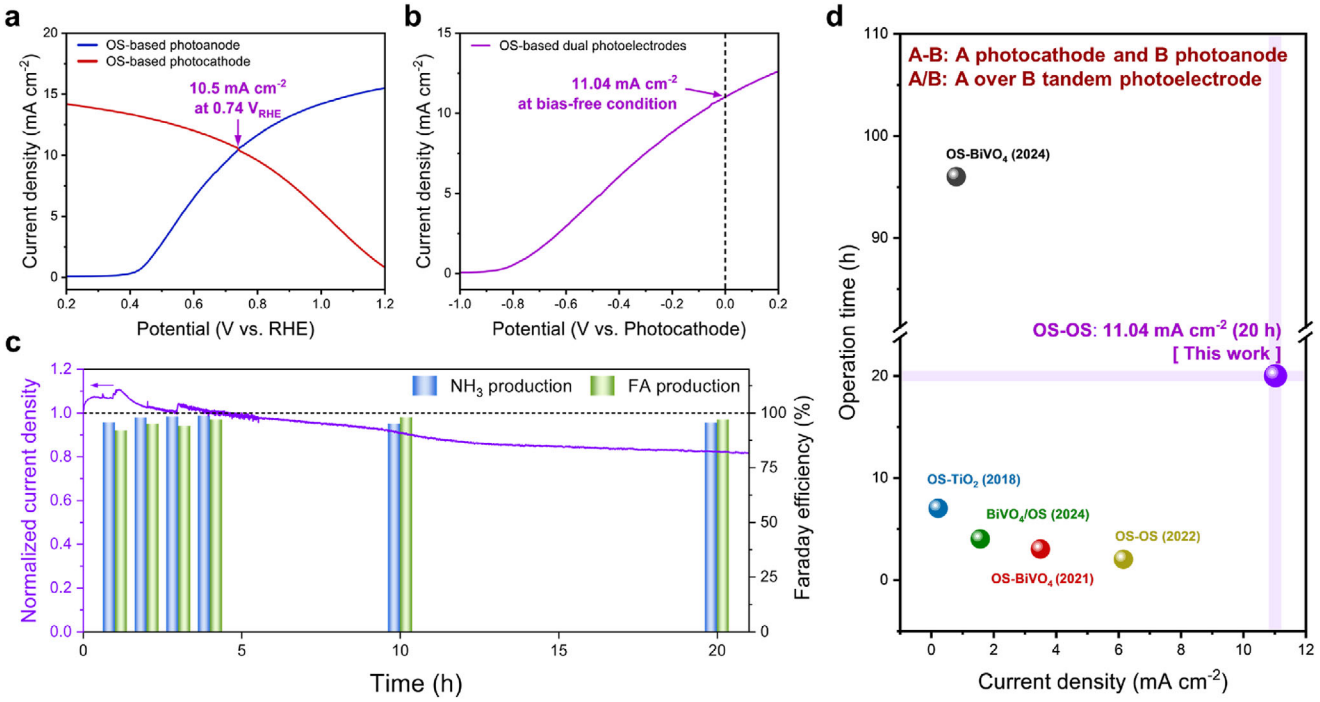

Figure 6. Performance of bias-free PEC solar upcycling system. a) Combined polarization curves of the OS-based photoanode and photocathode for expectation of the operating point of the dual-photoelectrodes system. b) Representative polarization curve of the OS-based dual photoelectrodes system using a two-electrode configuration with H-cell (1 M KOH + 0.1 M KNO_3 at the cathode side and 1 M KOH + 0.1 M glycerol at the anode side) at 50 mV s^{-1}. c) PEC stability of bias-free operation (0 V vs Photocathode) and Faraday efficiencies of upcycling reactions. d) Performance comparison of current research and previously reported works.

photoanode used as the working electrode and the photocathode as the counter electrode (counter electrode@reference electrode) (Figure S18, Supporting Information). All measurements were conducted using a Nafion-separated H-cell to eliminate potential cross-reactions or interference between oxidation and reduction products at each electrode. The anodic chamber was filled with 1 M KOH + 0.1 M glycerol, while the cathodic chamber contained 1 M KOH + 0.1 M KNO_3. To the best of our knowledge, a bias-free PEC solar-driven upcycling system for NO_3^- and glycerol utilizing OS-based dual-photoelectrodes has not been reported before.

The operating current density under sunlight illumination without any external bias can be estimated by the intersection point of the polarization curves of the photoanode and photocathode under closed-circuit conditions. Accordingly, the operating condition of the PEC upcycling system was predicted to be 10.5 mA cm^{-2} at 0.74 V_{RHE} (**Figure 6a**), a result attributed to the broad light absorption range of the OS photoabsorbers and the excellent charge separation and transport capabilities of the OS and charge transport layers (Figure S19a, Supporting Information). Measurement of the incident photon-to-current efficiency (IPCE) of the OS-based photoanode at the operating potential of 0.74 V_{RHE} confirmed excellent performance across a wide spectral range from 400 to 750 nm (Figure S19b, Supporting Information). In practical operation, the assembled two-electrode PEC upcycling system exhibited a high reaction current density of 11.04 mA cm^{-2} under bias-free condition (0 V vs Photocathode) (Figure 6b). The bias-free reaction current density slightly exceeds the predicted value due to the replacement of traditional half-cell reactions (OER@HER) with GOR at the photoanode and NO_3RR at the photocathode, which require lower overpotentials.[87,88] The operational stability of high current density upcycling system was evaluated under bias-free conditions with solar illumination (Figure 6c). The system retained 83% of its initial current density after 20 h of continuous operation. Compared to individual half-cell devices, the slightly lower stability in the dual-photoelectrodes configuration is attributed to the fact that the operating potential under bias-free conditions does not align with the maximum charge separation region. Such a mismatch leads to more frequent charge recombination within the devices, along with increased internal resistance and the formation of degradation sites upon photoelectrode integration.[89,90]

During operation, the photoanode carried out GOR, while the photocathode facilitated NO_3RR. Throughout 20 h of continuous operation, Faradaic efficiencies of over 95.0% for NH_3 and over 92.0% for FA were maintained (Figure 6c). The Faradaic efficiencies measured at 0.74 V_{RHE} in half-cell tests were consistent with those obtained from the bias-free PEC system, confirming the validity of the upcycling performance under integrated operation (Figure S20, Supporting Information). After 20 h, the FEs for NH_3 and FA were stably retained at 95.6% and 97.0%, respectively, confirming that the bias-free PEC system efficiently drives both NO_3RR and GOR upcycling under high current densities. The NH_3 production amounts obtained from electrochemical NO_3RR using Ni-Fe-P catalysts and from the bias-free PEC solar upcycling system were in close agreement when quantified via both UV-vis spectroscopy and ^1H NMR, validating the

reliability of the analytical methods employed in this study (Figure S21, Supporting Information). The OS-based bias-free system proposed in this study outperforms previously reported OS-based dual-photoelectrode or tandem bias-free PEC systems in terms of reaction current density (Figure 6d; Table S2, Supporting Information). Furthermore, considering that the current density of the OS-$BiVO_4$ bias-free system reported in 2024 dropped to nearly zero after 96 h of operation (retaining only ≈ 10% of its initial current density after 20 h), the system developed here can be considered one of the highest-performing OS-based PEC bias-free systems reported to date.[91–95]

3. Conclusion

In this study, a highly efficient and stable PEC upcycling system was developed by integrating Ni-Fe-P electrocatalysts with OS-based photoelectrodes. The Ni-Fe-P catalyst, synthesized via electrodeposition, exhibited excellent bifunctional activity for both GOR and NO_3RR, achieving high current densities and superior product selectivity. Through systematic comparison with Ni-P, Fe-P, and Ni-Fe catalysts, the synergistic effects of Ni, Fe, and P on electrocatalytic performance were clearly demonstrated. Using a metal foil encapsulation method with homemade carbon paste, the Ni-Fe-P/Cu foil was successfully coupled to OS-based OPV devices to construct photocathodes and photoanodes with high photoelectrochemical stability. The resulting OS-based dual-photoelectrode PEC system operated under bias-free conditions with 1 Sun illumination, achieving a high reaction current density of 11.04 mA cm^{-2}. Notably, the system showed sustained operation over 20 h, maintaining over 95% Faradaic efficiencies for NH_3 and FA production. Compared to previously reported OS-based PEC systems, the developed system demonstrated outstanding current density, selectivity, and long-term operational stability. This work provides a new strategy for solar-driven, sustainable upcycling of NO_3^- and glycerol, and highlights the potential of combining functional electrocatalysts with emerging organic photoelectrode technology in next-generation bias-free PEC systems. Importantly, the consistently high selectivity toward both NH_3 and FA not only reflects precise reaction control but also enhances its relevance for scalable and industrially viable solar chemical manufacturing. Furthermore, given the inherent scalability of organic semiconductor-based devices and the compatibility of our fabrication processes with large-area manufacturing techniques, this system holds significant promise for practical, large-scale PEC applications.

Supporting Information

Supporting Information is available from the Wiley Online Library or from the author.

Acknowledgements

This work was supported by the National Research Foundation of Korea (NRF) grant funded by the Korea Government (MSIT) (No. RS-2025-00563779). This research was supported by the Program of Future Hydrogen Original Technology Development (RS-2021-NR057808), through the National Research Foundation of Korea (NRF), funded by the Korean government. (Ministry of Science and ICT (MSIT)).

Conflict of Interest

The authors declare no conflict of interest.

Data Availability Statement

The data that support the findings of this study are available from the corresponding author upon reasonable request.

Keywords

artificial photosynthesis, bias-free system, glycerol oxidation reaction, nitrate reduction reaction, organic semiconductors, photoelectrochemistry, solar upcycling

Received: April 23, 2025
Revised: July 1, 2025
Published online:

[1] I. E. Agency, in *World Energy Outlook 2023*, IEA, Paris **2023**.
[2] S. N. Naik, V. V. Goud, P. K. Rout, A. K. Dalai, *Renewable Sustainable Energy Rev.* **2010**, *14*, 578.
[3] T. Hassan, M. M. Rahman, M. A. Rahman, M. N. Nabi, *Biofuels, Bioproducts Biorefining* **2022**, *16*, 1353.
[4] T. Lin, L. F. Rodríguez, S. Davis, M. Khanna, Y. Shastri, T. Grift, S. Long, K. C. Ting, *GCB Bioenergy* **2016**, *8*, 160.
[5] Y. Gao, A. C. Serrenho, *Nat. Food* **2023**, *4*, 170.
[6] M. R. Monteiro, C. L. Kugelmeier, R. S. Pinheiro, M. O. Batalha, A. da Silva César, *Renew. Sustain. Energy Rev.* **2018**, *88*, 109
[7] E. Craswell, *SN Appl. Sci.* **2021**, *3*, 518.
[8] P. H. van Langevelde, I. Katsounaros, M. T. M. Koper, *Joule* **2021**, *5*, 290.
[9] C. M. G. Andrade, S. I. Gomes, M. A. S. S. Ravagnani, E. L. Almeida, in *Biotechnological Applications of Biomass*, (Eds: T. Peixoto Basso, T. O. Basso, L. C. Basso), IntechOpen, Rijeka **2021**.
[10] H. Huang, K. Peramaiah, K.-W. Huang, *Energy Environ. Sci.* **2024**, *17*, 2682.
[11] H. M. A. Sharif, H. M. F. Khan, S. Ullah, Y. Wang, M. Ahmad, B.o Yang, C. Li, M. B. Asif, *J. Energy Chem.* **2024**, *95*, 380.
[12] L. Luo, W. Chen, S.i-M. Xu, J. Yang, M. Li, H. Zhou, M. Xu, M. Shao, X. Kong, Z. Li, H. Duan, *J. Am. Chem. Soc.* **2022**, *144*, 7720.
[13] L. Fan, B. Liu, X. Liu, N. Senthilkumar, G. Wang, Z. Wen, *Energy Technol.* **2021**, *9*, 2000804.
[14] F. Liu, J. Zhou, M. Sun, Z. Xu, H. Wang, N. Yao, Y. Wang, F. Hao, Y. Xiong, J. Wang, L. Guo, Q. Wa, G. Wang, X. Meng, M. Shao, C. Wang, H. C. Chen, H. M. Chen, Y. Zhu, B. Huang, Z. Fan, *Angew. Chem.* **2025**, *137*, 202504641.
[15] Y. Wang, Y. Xiong, M. Sun, J. Zhou, F. Hao, Q. Zhang, C. Ye, X. Wang, Z. Xu, Q. Wa, F. Liu, X. Meng, J. Wang, P. Lu, Y. Ma, J. Yin, Y. Zhu, S. Chu, B. Huang, L. Gu, Z. Fan, *Angew. Chem.* **2024**, *136*, 202402841.
[16] Y. Xiong, Y. Wang, M. Sun, J. Chen, J. Zhou, F. Hao, F.u Liu, P. Lu, X. Meng, L. Guo, Y. Liu, S. Xi, Q. Zhang, B. Huang, Z. Fan, *Adv. Mater.* **2024**, *36*, 2407889.
[17] Y. Xiong, Y. Wang, J. Zhou, F. Liu, F. Hao, Z. Fan, *Adv. Mater.* **2024**, *36*, 2304021.
[18] G. Dodekatos, S. Schünemann, H. Tüysüz, *ACS Catal.* **2018**, *8*, 6301.
[19] W. Zhong, Q.-L. Hong, X. Ai, C. Zhang, F.-M. Li, X.-F. Li, Y. Chen, *Adv. Mater.* **2024**, *36*, 2314351.
[20] Y. Wang, M. Sun, J. Zhou, Y. Xiong, Q. Zhang, C. Ye, X. Wang, P. Lu, T. Feng, F. Hao, F. Liu, J. Wang, Y. Ma, J. Yin, S. Chu, L. Gu, B. Huang, Z. Fan, *Proc. Natl. Acad. Sci. USA* **2023**, *120*, 2306461120.

[21] Y. Jung, S. Kim, H. Choi, Y. Kim, J. B. Hwang, D. Lee, Y. Kim, J.-C. Park, D.-Y. Kim, S. Lee, *Nanomaterials* **2023**, *13*, 1690.
[22] J.-X. Liu, D. Richards, N. Singh, B. R. Goldsmith, *ACS Catal.* **2019**, *9*, 7052.
[23] W. Chen, L. Zhang, L. Xu, Y. He, H. Pang, S. Wang, Y. Zou, *Nat. Commun.* **2024**, *15*, 2420.
[24] K. Su, S. Ren, R. T. Gao, G. E. Bai, L. Wu, L. Wang, *Angew. Chem., Int. Ed.* **2025**, *64*, 202422443.
[25] H. Chen, R. T. Gao, K. Su, Z. Li, L. Wu, L. Wang, *Angew. Chem.* **2025**, *137*, 202501766.
[26] L. Xie, L. Hu, Q. Liu, S. Sun, L. Zhang, D. Zhao, Q. Liu, J. Chen, J. Li, L. Ouyang, A. A. Alshehri, Q. Kong, X. Sun, *Inorg. Chem. Front.* **2022**, *9*, 3392.
[27] Y. Yao, K. Wei, S. Zhao, H. Zhou, B. Kui, G. Zhu, W. Wang, P. Gao, W. Ye, *ACS Sustain. Chem. Eng.* **2025**, *13*, 1245.
[28] D. Kim, C. D. Van, M. S. Lee, M. Kim, M. H. Lee, J. Oh, *ACS Catal.* **2024**, *14*, 7717.
[29] Y. Han, M. Chang, Z. Zhao, F. Niu, Z. Zhang, Z. Sun, L. Zhang, K. Hu, *ACS Appl. Mater. Interfaces* **2023**, *15*, 11678.
[30] C. S. Santana, E. Gjonaj, A. C. Garcia, *ChemElectroChem* **2024**, *11*, 202300570.
[31] X. Chen, T. Zhang, M. Kan, D. Song, J. Jia, Y. Zhao, X. Qian, *Environ. Sci. Technol.* **2020**, *54*, 13344.
[32] L.-A. Stern, L. Feng, F. Song, X. Hu, *Energy Environ. Sci.* **2015**, *8*, 2347.
[33] Q. Zhang, T. Li, J. Liang, N. Wang, X. Kong, J. Wang, H. Qian, Y. Zhou, F. Liu, C. Wei, Y. Zhao, X. Zhang, *J. Mater. Chem. A* **2018**, *6*, 7509.
[34] S. Jo, B. Kang, H. Oh, J. Kwon, P. Choi, K.-Y. Cho, J.-H. Lee, K. Eom, *Chem. Eng. J.* **2023**, *457*, 141138
[35] Q. Yao, J. Chen, S. Xiao, Y. Zhang, X. Zhou, *ACS Appl. Mater. Interfaces* **2021**, *13*, 30458.
[36] S. Ye, Z. Chen, G. Zhang, W. Chen, C. Peng, X. Yang, L. Zheng, Y. Li, X. Ren, H. Cao, D. Xue, J. Qiu, Q. Zhang, J. Liu, *Energy Environ. Sci.* **2022**, *15*, 760.
[37] D. Li, H. Gong, L. Lin, W. Ma, Q. Zhou, K. Kong, R. Huang, Z. Hou, *Mol. Catal.* **2019**, *474*, 110404
[38] M. Grätzel, *Nature* **2001**, *414*, 338.
[39] Z. Li, W. Luo, M. Zhang, J. Feng, Z. Zou, *Energy Environ. Sci.* **2013**, *6*, 347.
[40] R. T. Gao, Z. Gao, N. T. Nguyen, J. Chen, X. Liu, L. Wang, L. Wu, *Nat. Sustain.* **2025**, *6*, 672.
[41] R. T. Gao, Y. Yang, X. Liu, X. Zhang, L. Wang, L. Wu, *Matter* **2024**, *7*, 2278.
[42] R. T. Gao, N. T. Nguyen, T. Nakajima, J. He, X. Liu, X. Zhang, L. Wang, L. Wu, *Sci. Adv.* **2023**, *9*, ade4589.
[43] Y. Jung, S. Kim, S. Kim, Y. Kim, J. B. Hwang, D.-Y.u Kim, S. Lee, *Small* **2025**, *21*, 2409082.
[44] L. Yao, A. Rahmanudin, N. Guijarro, K. Sivula, *Adv. Energy Mater.* **2018**, *8*, 1802585.
[45] J. M. Yu, J.-W. Jang, *Catalysts* **2023**, *13*, 814.
[46] J. Park, K. H. Kim, D. Kim, J. K. Kim, W. Yang, *Sustain. Energy Fuels* **2024**, *8*, 481.
[47] S. Seo, J.-H. Lee, Y. Kim, S. Kim, C. J. Yoon, H. Choi, S. Lee, K. Lee, H. Kim, S. Lee, *J. Mater. Chem. A* **2022**, *10*, 13247.
[48] A. Wadsworth, H. Bristow, Z. Hamid, M. Babics, N. Gasparini, C. W. Boyle, W. Zhang, Y. Dong, K. J. Thorley, M. Neophytou, R. S. Ashraf, J. R. Durrant, D. Baran, I. McCulloch, *Adv. Funct. Mater.* **2019**, *29*, 1808429.
[49] Q. Tu, C. Tang, Q. Zheng, *J. Mater. Chem. A* **2019**, *7*, 3307.
[50] F. L. Araújo, D. R. B. Amorim, B. B. M. Torres, D. J. Coutinho, R. M. Faria, *Sol. Energy* **2020**, *208*, 583.
[51] E. Çokduygulular, Ç. Çetinkaya, S. Emik, B. Kınacı, *Sci. Rep.* **2023**, *13*, 7548.
[52] J. H. Jeong, M. Jahandar, A. Prasetio, J. M. Kim, J. H. Kim, S. Kim, D. C. Lim, *Chem. Eng. J.* **2021**, *419*, 129672
[53] J. O. Silva, S. Cartagena, J. A. Calderón, *Electrochim. Acta* **2023**, *451*, 142299
[54] S. Carenco, D. Portehault, C. Boissiere, N. Mezailles, C. Sanchez, *Chem. Rev.* **2013**, *113*, 7981.
[55] P. E. Blanchard, A. P. Grosvenor, R. G. Cavell, A. Mar, *Chem. Mater.* **2008**, *20*, 7081.
[56] L. Zhang, R. K. Brow, *J. Am. Ceram. Soc.* **2011**, *94*, 3123.
[57] K. D. Litasov, N. M. Podgornykh, *J. Raman Spectrosc.* **2017**, *48*, 1518.
[58] Y. Du, Y. Han, X. Huai, Y. Liu, C. Wu, Y. Yang, L. Wang, *Int. J. Hydrogen Energy* **2018**, *43*, 22226.
[59] A. Muthurasu, T. H. Ko, T. W. Kim, K. Chhetri, H. Y. Kim, *Adv. Funct. Mater.* **2024**, *34*, 2404254.
[60] Z. Wei, M. Guo, Q. Zhang, *Appl. Catal., B* **2023**, *322*, 122101
[61] L.-H. Xu, P.-C. Che, X.-J. Zhang, S. Cosnier, D. Shan, *Appl. Surf. Sci.* **2023**, *620*, 156770
[62] T. Wang, C. Zhao, L. Meng, Y. Li, D. Wang, C.-C. Wang, *Appl. Catal. B: Environ.* **2023**, *334*, 122832.
[63] Y. Gao, Z. Chen, Y. Zhao, W. Yu, X. Jiang, M. He, Z. Li, T. Ma, Z. Wu, L. Wang, *Appl. Catal. B: Environ.* **2022**, *303*, 120879.
[64] X. Zhou, H. Gao, Y. Wang, Z. Liu, J. Lin, Y. Ding, *J. Mater. Chem. A* **2018**, *6*, 14939.
[65] M. K. Goetz, M. T. Bender, K.-S. Choi, *Nat. Commun.* **2022**, *13*, 5848.
[66] A.-E. Radi, W. F.-D. Ashour, R. Elshafey, *Electrocatalysis* **2022**, *13*, 653.
[67] D. Guo, J. Qi, W. Zhang, R. Cao, *ChemSusChem* **2017**, *10*, 394.
[68] Y. Zheng, Z. Kang, H. Li, X. Song, W. Zhang, G. Wang, X. Tao, *Adv. Funct. Mater.* **2025**, *35*, 2412810.
[69] Y. Yan, R. Wang, Q. Zheng, J. Zhong, W. Hao, S. Yan, Z. Zou, *Nat. Commun.* **2023**, *14*, 7987.
[70] I. Chauhan, P. M. Vijay, R. Ranjan, K. K. Patra, C. S. Gopinath, *ACS Mater. Au* **2024**, *4*, 500.
[71] L. Liu, K. Jia, W. Su, H. Zhao, Z. Huang, G. Wang, W. Fan, R. Zhang, H. Bai, *Inorg. Chem.* **2024**, *63*, 2756.
[72] Y. Bai, Z. Fang, Y. Lei, L. Liu, H. Zhao, H. Bai, W. Fan, W. Shi, *Green Energy Environ.* **2024**, *9*, 1112.
[73] W. Yang, Z. Chang, X. Yu, et al., *Angew. Chem., Int. Ed.* **2024**, *64*, 202415300.
[74] J. Yan, J. Li, P. Liu, H. Huang, W. Song, *Green Chem.* **2023**, *25*, 8645.
[75] K. Qu, X. Zhu, L. Song, J. Wang, Y. Gong, X. Liu, S. Yuan, Q. Lu, Y. Yu, A.-L. Wang, *Chem. Eng. J.* **2025**, *510*, 161814.
[76] Q. Hu, C. Shang, X. Chen, S. Qi, Q. Huo, H. Yang, C. He, *J. Am. Chem. Soc.* **2025**, *147*, 12228.
[77] R. Gao, J. Zhang, G. Fan, X. Wang, F. Ding, Y. Guo, C. Han, Y. Gao, A. Shen, J. Ding, L. Wu, X. Gu, *Angew. Chem., Int. Ed.* **2025**, https://doi.org/10.1002/anie.202505948.
[78] X. Shi, M. Xie, K. Yang, Y. Niu, H. Ma, Y. Zhu, J. Li, T. Pan, X. Zhou, Y. Cui, Z. Li, Y. Yu, X. Yu, J. Ma, H. Cheng, *Angew. Chem., Int. Ed.* **2024**, *63*, 202406750.
[79] W. Zheng, L. Zhu, Z. Yan, Z. Lin, Z. Lei, Y. Zhang, H. Xu, Z. Dang, C. Wei, C. Feng, *Environ. Sci. Technol.* **2021**, *55*, 13231.
[80] H. C. Rojas, S. Bellani, F. Fumagalli, G. Tullii, S. Leonardi, M. T. Mayer, M. Schreier, M. Grätzel, G. Lanzani, F. Di Fonzo, M. R. Antognazza, *Energy Environ. Sci.* **2016**, *9*, 3710.
[81] L. Yao, N. Guijarro, F. Boudoire, Y. Liu, A. Rahmanudin, R. A. Wells, A. Sekar, H.-H. Cho, J.-H. Yum, F. Le Formal, K. Sivula, *J. Am. Chem. Soc.* **2020**, *142*, 7795.
[82] T. Bourgeteau, D. Tondelier, B. Geffroy, R. Brisse, R. Cornut, V. Artero, B. Jousselme, *ACS Appl. Mater. Interfaces* **2015**, *7*, 16395.
[83] A. Mezzetti, F. Fumagalli, A. Alfano, D. Iadicicco, M. R. Antognazza, F. di Fonzo, *Faraday Discuss.* **2017**, *198*, 433
[84] T. H. Lee, R. R. Rao, R. A. Pacalaj, A. A. Wilson, J. R. Durrant, *Adv. Energy Mater.* **2022**, *12*, 2103698.
[85] J. M. Yu, J. Lee, Y. S. Kim, J. Song, J. Oh, S. M. Lee, M. Jeong, Y. Kim, J. H. Kwak, S. Cho, C. Yang, J.-W. Jang, *Nat. Commun.* **2020**, *11*, 5509.

[86] W. Shi, D. Li, D. Tu, D. Li, W. Yu, J. Shi, C. Li, *Adv. Funct. Mater.* **2023**, *33*, 2209211.
[87] O. Q. Carvalho, R. Marks, H. K. K. Nguyen, M. E. Vitale-Sullivan, S. C. Martinez, L. Árnadóttir, K. A. Stoerzinger, *J. Am. Chem. Soc.* **2022**, *144*, 14809.
[88] C. Minero, A. Bedini, V. Maurino, *Appl. Catal., B* **2012**, *128*, 135
[89] F. Nandjou, S. Haussener, *J. Phys. D: Appl. Phys.* **2017**, *50*, 124002.
[90] J. H. Kim, J.i-W. Jang, Y. H. Jo, F. F. Abdi, Y. H. Lee, R. van de Krol, J. S. Lee, *Nat. Commun.* **2016**, *7*, 13380.
[91] C. W. S. Yeung, V. Andrei, T. H. Lee, J. R. Durrant, E. Reisner, *Adv. Mater.* **2024**, *36*, 2404110.
[92] D. Shao, L. Zheng, D. Feng, J. He, R. Zhang, H. Liu, X. Zhang, Z. Lu, W. Wang, W. Wang, F. Lu, H. Dong, Y. Cheng, H. Liu, R. Zheng, *J. Mater. Chem. A* **2018**, *6*, 4032.
[93] C. G. Ferreira, C. Sansierra, F. Bernal-Texca, M. Zhang, C. Ros, J. Martorell, *Energy Environ. Mater.* **2024**, *7*, 12679.
[94] S. Ye, W. Shi, Y. Liu, D. Li, H. Yin, H. Chi, Y. Luo, N.a Ta, F. Fan, X. Wang, C. Li, *J. Am. Chem. Soc.* **2021**, *143*, 12499.
[95] D. Zhang, H.-H. Cho, J.-H. Yum, M. Mensi, K. Sivula, *Adv. Energy Mater.* **2022**, *12*, 2202363.